Solution Treatment Study of Inconel 718 Produced by SLM Additive Technique in View of the Oxidation Resistance

DOI: 10.1002/adem.201800351

Solution Treatment Study of Inconel 718 Produced by SLM Additive Technique in View of The Oxidation Resistance **

By *Michele Calandri, Diego Manfredi, Flaviana Calignano, Elisa Paolo Ambrosio, Sara Biamino, Rocco Lupoi, Daniele Ugues**

[*] *Dr. M. Calandri*
Dipartimento di Scienza Applicata e Tecnologia (DISAT), Politecnico di Torino
Corso Duca degli Abruzzi, 24, 10129, Turin, Italy
E-mail: michele.calandri@polito.it
Dr. D. Manfredi
Center for Sustainable Futures Technologies-CSFT@POLITO, Istituto Italiano di Tecnologia
Via Livorno, 60, 10144, Turin, Italy
E-mail: Diego.Manfredi@iit.it
Dr. F. Calignano
Dipartimento di Ingegneria Gestionale e della Produzione (DIGEP), Politecnico di Torino
Corso Duca degli Abruzzi, 24, 10129, Turin, Italy
E-mail: flaviana.calignano@polito.it
Dr. E. P. Ambrosio
Center for Sustainable Futures Technologies-CSFT@POLITO, Istituto Italiano di Tecnologia
Via Livorno, 60, 10144, Turin, Italy
E-mail: Elisa.Ambrosio@iit.it
Prof. Dr. S. Biamino
Dipartimento di Scienza Applicata e Tecnologia (DISAT), Politecnico di Torino
Corso Duca degli Abruzzi, 24, 10129, Turin, Italy
E-mail: sara.biamino@polito.it
Prof. Dr. R. Lupoi
Trinity College Dublin, The University of Dublin, Department of Mechanical and Manufacturing Engineering, Parsons Building, Dublin 2, Ireland
E-mail: LUPOIR@tcd.ie>
Prof. Dr. D. Ugues
Dipartimento di Scienza Applicata e Tecnologia (DISAT), Politecnico di Torino
Corso Duca degli Abruzzi, 24, 10129, Turin, Italy
E-mail: daniele.ugues@polito.it

[**] *The research leading to part of these results has received funding from the European Union's Seventh Framework Programme for the Fuel Cells and Hydrogen Joint Technology Initiative under grant agreement n° 621210 for the HELMETH project (Integrated High-Temperature Electrolysis and Methanation for Effective Power to Gas Conversion).*

The additive manufacturing concept for the production of complex near net shape metal parts is obtaining increasing attention due to the possibility of producing assembled and/or complex parts allowing optimal design and saving time and cost. The possibility to use the free design of Selective Laser Melting (SLM) techniques for the fabrication of complex 3D components using high performing, although difficult to work, materials such as Ni superalloys is really attractive.

The particular process conditions that are established during additive manufacturing in SLM leads to microstructures different with respect to those observed in standard cast or wrought analogous material. Therefore it is usually necessary to apply a post solution treatment, in order to reduce the segregation of heavier elements (in particular Nb) and dissolve the interdendritic precipitates.

In this study the influence of temperature and time of the solution treatment on the microstructure is investigated in order to find the best results in terms of the final oxidation resistance. Oxidation performances of solutioned Inconel 718 fabricated via SLM are reported and discussed. The growth rate of the superficial oxide at the temperature of 850 °C was measured and the long-term stability of this passivating layer was tested until 908 hours.

1. Introduction

Selective Laser Melting (SLM) is a powder bed Additive Manufacturing (AM) technique that allows to produce geometrical complex parts avoiding welds or further joining processes.[1] [2] The additive manufacturing strategy is becoming more and more interesting for the production of near net shape metal parts in small series due to the opportunity of a significant reduction of time and cost of the design step.[3] The high freedom of design allowed by SLM could be useful in many high temperature applications, for example in the fields of energy production, chemical plants or aerospace. In these applications, the constitutive materials operate at high temperatures

for long time exposure, thus good properties of thermal resistance, in particular an elevated resistance to hot oxidation, are required.

For this purpose Inconel 718 is a nickel alloy that has good oxidation behavior also at very high temperature (typically 650-700 °C and even at around 900 °C).[4] [5]

This material has a very complex multiphase microstructure, that is composed by the γ matrix and by many different kinds of intergranular or transgranular precipitates whose distribution and size depend on the solidification condition and the following heat treatments. The main compounds that can be found are MC-type carbides (usually NbC), $(Ni,Cr,Fe)_2(Nb,Mo,Ti)$ Laves phases, δ (Ni_3Nb) orthorhombic intermetallic phase and the γ' or γ'' strengthening intermetallics.[6] [7]

The standard Inconel 718 heat treatment recipe includes a solution step and an aging step. During solutioning the provided heat dissolves the precipitates and so most of the alloying elements are released into solid solution. The material is then rapidly cooled through air or water quenching in order to avoid further precipitation. Strengthening phases like γ'-$Ni_3(Ti,Al)$ or γ''-Ni_3Nb precipitates from the supersaturated solid solution during the aging step.[8] The temperature range used in the solution treatment of Inconel 718 are usually between 920 °C and 1070 °C, being the typically applied soaking time about 1 hour. After solutioning a double aging treatment is usually performed to promote fine precipitates formation and to optimize the mechanical properties.

The two standard recipes of heat treatments and the related parameters according to Aerospace Material Specifications (AMS) 5662-3-4 are:[9]

- solutioning at 980°C for 1 hour; air or argon cooling; aging treatment consisting in a soaking step at 720 °C for 8 hours, followed by a slow cooling step performed into the furnace that takes 2 hours from 720 °C to 620 °C and a consequent soaking at this tempearature for 8 hours; final air or argon cooling down to room temperature;

- solutioning at 1065 °C for 1 hour; air or argon cooling; aging treatment consisting in a soaking at 760 °C for 10 hours, followed by a slow cooling step performed into the furnace that takes 2 hours from 760 °C to 650 °C and a consequent soaking at this tempearature for 8 hours; final air or argon cooling down to room temperature.

With respect to conventional fabrication routes the SLM technique involves instantaneous local melts of the powders and subsequent very rapid cooling and solidification that lead to the formation of anisotropy[10] and non-equilibrium states.[11] However, during the forming process the deposited layers are also subjected to a series of thermal cycles due to the heat provided by the subsequent laser scans:[12] whenever a new layer is added, a partial re-melting of the previously deposited layers occurs. Furthermore, a thermally affected zone forms below the re-melted portion like in a welding process. As a consequence of the complex and non-uniform thermal history followed by the material, all the previously listed types of precipitates can potentially form already during the SLM process and the final microstructure can highly differ from the ones typically obtained in the conventional fabrication processes.[13] [14] [15] [16] [17] [18] For that reason, also the response to the solution treatment can be much different from that provided on traditionally fabricated alloys. Actually, the particular initial conditions of the material characterized by anisotropy, residual stress states, fine microstructure and marked micro-segregation patterns can require to define a completely new solutioning recipe.[19] [20] [21] [22]

Within the present research the Inconel 718 fabricated via additive manufacturing was studied for a specific final application, that is the development of a heat exchanger devoted to continuously work at 850°C in heavy oxidative environment.[23] Part of the research on material, preliminary to the component fabrication, is reported hereby. According to the ultimate service application, the requirements for the AM material to be fabricated was to guarantee long term oxidation resistance for continuous operating mode at 850°C, with limited requests on structural

resistance, as the heat exchanger will be subjected to light combined thermal and mechanical loads. For such reason, the set-up of the optimal heat treatment recipe to be applied on SLM Inconel 718 was focused only on the solutioning parameters. This decision was taken also considering that the service operating temperature would be rather high with respect to any aging treatment, thus providing a sort of service aging that would modify the artificial aged microstructure. Both holding time and temperature were studied with the aim of properly solutioning the residual as built precipitation structures.

To validate the developed solutioning recipe, the growth rate of the thermally grown oxide formed on SLM Inconel 718 alloy, previously submitted to the defined optimal heat treatment, was finally studied upon prolonged exposition at 850°C. Conclusions on oxidation mechanisms, oxide layers composition and their microstructure are also given.

2. Experimental procedures

A commercial Inconel 718 powder (EOS GmbH, Germany[9]) produced by gas atomizing process was used. The nominal chemical composition is reported in **table 1**. The samples were removed from bars fabricated using an EOSINT M270 Dual mode machine, equipped with 200W Yb fiber continuous laser beam with a focused diameter of 100 μm and a set layer thickness of 20 μm.

The building parameters for the SLM fabrication were as followed:

- laser power: 195 W
- scan velocity: 1200 mm/s
- hatching distance: 0.09 mm
- spot size: 100 μm

These parameters were selected according to preliminary process set up trials, devoted to minimize cracks and pores occurrence.

The test coupons used for the research were built starting from a stainless steel base plate. Once the SLM production job was completed, test coupons still attached to the supported base plate were subjected to stress relieving, 450°C for 2 h. After that they were removed from the support plate by mechanical cutting.

Solutioning trials were performed using a BICASA mod B.E. 35 muffle furnace. The samples were introduced in the pre-heated chamber of the furnace and held at a steady test temperature in air for a fixed period of time, then rapidly cooled with water quenching to prevent precipitation that can occur during the cooling stage. The details of the investigated solutioning recipes are reported in **table 2**.

The 980 and 1065 °C are standard solution temperatures proposed in the reference heat treatment guides as discussed earlier. On the contrary, the 1200 °C is not typically proposed for such alloy, but it was here considered with the aim of investigating an upper boundary of solutioning stage. The two hours treatment, which is not typically applied on traditionally fabricated Inconel 718, was investigated in view of the very high stability of as built SLM microstructural features, as discussed below.

The samples were then polished with successive grades of SiC polishing paper in order to remove the superficial formed oxide and all the sub-superficial layers that could be affected by internal oxidation during the heat treatment.

The microstructures of the solutioned samples were characterized by Optical Microscopy (OM, Leica DMI 5000 M) and Field Emission Scanning Electron Microscopy (FESEM, Zeiss SupraTM 40). The size and volume fraction of the detected phases were assessed through image analysis process according to the procedure described below. All the samples observed were previously polished with diamond pastes until 1 μm grade and then chemically etched with waterless Kalling's reagent (5 g $CuCl_2$ in 100 ml HCl and 100 ml ethanol).

The taken Secondary Electrons (SE) FESEM images were analyzed in order to get an average value of the volume fraction of the precipitates (given by the ratio between the area occupied

by the precipitates and the total image area) and also the size distribution of the precipitates in the solutioned state. This analysis was performed, where possible, by distinguishing the different types of precipitates according to their morphology. For untreated samples six SE FESEM images per sample were analyzed: two images taken at 25 kX magnification (covering a total area of 152.1 μm^2), two images at 75 kX (covering a total area of 16.7 μm^2) and two images at 150 kX (covering a total area of 4.2 μm^2). Therefore, an overall area of 346 μm^2 was used for this analysis. The precipitates in heat-treated samples were evaluated through the analysis of five images per sample taken at 25 kX magnification and five images taken at 75 kX each. Therefore, in this case an overall area of 844 μm^2 was used for this analysis. All the detected precipitates in these samples were classified according to their linear size, L, defined as:

$$L\,[nm] = 1000 \cdot \sqrt{M\,\left[\frac{\mu m^2}{pixel}\right] \cdot P} \qquad (1)$$

where P is extension of the single precipitate in terms of number of pixels and M is the length scale of the image, i.e. the real area extension of a single pixel.

Vickers microhardness measurements were also recorded using a Microhardness Tester VMHT with Leica Camera to preliminary investigate the influence of the heat treatment on the mechanical properties of the alloy. The measurements were performed imposing a normal load of 100 gf for 15 seconds. The purpose of this test was mainly to indirectly assess the level of precipitates solutioning provided by the different heat treatment trials.

According to the results of the heat treatment trials, the most promising solutioning recipe was applied on a new set of samples that were used to evaluate the oxidation resistance achieved by SLM solutioned Inconel 718. After solutioning, samples were polished, cleaned and then weighed prior to start the oxidation runs. The complete set of prepared samples were then placed into an atmospheric furnace, with controlled temperature deviations at different locations within ±10°C. At the beginning of the oxidation test run, the samples were heated at 850 °C into a

muffle furnace with air environment. At predetermined increasing exposure times, one sample per exposure time was then removed from the furnace and cooled in calm air down to room temperature. The last two samples were removed together after 351 hours of exposition. The mass change of samples subjected to this isothermal oxidation test run was measured with a precision balance with 0.1 mg resolution.

In order to study the mass change behavior for longer time of oxidation at 850°C, a second oxidation procedure was applied using the two samples removed from the furnace after 351 hours. After the weighing step these two samples were again introduced into the furnace and exposed at 850 °C for longer times. By this way two further exposition steps at 850°C could be studied: 755 and 908 hours.

Finally, the oxidized samples were cut along cross section and prepared with the same metallographic procedure as described above, to investigate the thermally grown oxide nature and morphology. To this purpose, Optical Microscopy (OM), Field Emission Scanning Microscopy (FESEM, Merlin Zeiss) and semi-quantitative Energy Dispersive Spectroscopy (EDS) analysis were applied.

3. Results and Discussion

3.1. Microstructural analysis

3.1.1. As built Microstructure

Grain morphology on as built samples is highly anisotropic when observed along the plane of the deposited powder layers (referred as xy plane) and along the plane parallel to the building direction (referred as z plane). The parallel tracks formed during the laser scan are much evident on the xy plane (**figure 1-a**). On the contrary, the predominant structural features on the z planes are the typical arc-shaped and partially overlapped melt pools contours. They derive from local melting of the irradiated zone and subsequent rapid solidification as soon as the laser spot

moves far from that area (**figure 1-b**). These microstructural features are typical of additive manufacturing processes.[24] [25] [26]

The general microstructure of the as built sample is characterized by elongated grains that develop along the building direction (z). It can be observed that the lying of grains boundaries (white arrows in **figures 1-c** and **1-d**) is independent by the laser formed pool contours (red arrows in **figure 1**) and that a single grain usually grows through more than one melt pool. This is in agreement with other observations reported in literature.[10] [14] [20] [27] [28] [29] [30] [31] [32] [33] [34] The solidification of the melt pools occurs mainly through the epitaxial growth of the grains at the solid/liquid interface rather than by nucleation of new grains, leading to the formation of relatively coarse and columnar grains that cross several deposited layers maintaining their own crystallographic orientation.[30] [35]

Within the core of each grain a very fine sub-structure develops, consisting of strongly oriented patterns approximately parallel to the building direction (thus perpendicular to the x-y plane). This intragranular texture consists of very narrow columnar dendrites limited by interdendritic segregated zones (dark areas in the optical micrographs of figures 1-c and 1-d) and forms a fine cellular microstructure. Such microstructure derives from the particular conditions, which are established during the SLM process.[20] In particular, the extremely rapid cooling of the melt pool and the thermal gradients that forms during solidification are major causes for this.[36] [37]

Once this extremely fine cellular dendritic microstructure was studied at higher magnifications with FESEM (**figure 2**), provided evidences that different populations of precipitates were formed during the building process. This gives clues to the fact that actually different segregation processes had occurred during Inconel 718 consolidation via SLM. Actually, homogeneously dispersed intradendritic nanometric precipitates (dark greys spots within red dotted circles in figure 2-c), and either irregular (white spots within brown dotted circles in figure 2-c) or globular (light greys spots within black dotted circles in figure 2-c) coarser interdendritic precipitates can be detected. According to the discussion reported below inter-

dendritic precipitates are expected to be Laves phases (brown circles) and carbides (black circles).

The concept of the partition coefficient, *k*, between the liquid and the solid phases of the main alloy elements can be used to clarify the segregation phenomena that occur during solidification.[38] The elements very miscible in nickel, i.e. iron and chromium, have a value of *k* greater than one, this means that Cr and Fe tend to dissolve most in the solid than in the liquid. On the contrary, niobium, molybdenum and titanium are less soluble in nickel and have a value of *k* lower than one. Therefore, these latter elements tend to segregate in the residual liquid phase during solidification at inter-dendritic regions. Actually, since in SLM route solidification takes place very quickly, diffusion in the solid phase has not time enough to occur. Therefore, the mean composition of the forming dendrite becomes richer in elements with $k > 1$ (Cr and Fe) and poorer in the ones with $k < 1$ (Nb, Mo and Ti) with respect to the nominal concentration values in thermodynamic equilibrium conditions. The surplus of elements characterized by a partition coefficient lower than 1 as solidification proceeds is, thus, progressively rejected into the residual liquid at interdendritic regions. According to Knorovsky et al.[39] the solidification of Inconel 718 in non-equilibrium conditions ends with two not invariant eutectic transformations. First the L → L + γ + carbides (NbC) transformation occurs, with a consequent depletion of Nb and C from the liquid phase. This transformation proceeds until the carbon is completely depleted from liquid. Thus, in the final solidification stage the γ phase continues to form causing a re-enrichment of Nb, Mo and Ti in the liquid and, as a consequence, at last the L → γ + Laves transformation occurs.[40] [41] These eutectic products don't form the typical eutectic lamellar structure, but give rise to the so-called divorced eutectic[21], that is a mixture in which the minor phases (carbides and Laves) appears in the form of isolated precipitates and the formation of the major phase (the γ matrix) has the effect of a thickening of the already formed dendrites.[42] The above described solidification process of SLM Inconel 718 is schematically resumed in figure 2-a and related to the sequence of progressive solidification

steps and to the occurrence of the eutectic transformations. By observing such schematics, one can easily locate the regions where solidification occurs earlier (intra-dendritic areas), regions where solidification occurs at intermediate periods (inter-dendritic thin boundaries between two adjacent dendrites) and regions where solidification occurs later (inter-dendritic triple points where three adjacent dendritic cells are in contact).[43] Therefore, according to these considerations and having in mind the locations where different precipitates were detected, one can conclude that small globular precipitates observed along the thin inter-dendritic regions (figure 2-c) are carbides, whereas the relative coarse precipitates of irregular shape formed at thicker inter-dendritic triple points of intersection between cells are Laves phases. This kind of as built microstructure with the presence of Laves phases and carbides at different locations is also reported in other studies.[21] [22] [33] Brenne et al. also identified Laves phases in the as built state of SLM Inconel 718 using EDS and TEM techniques.[44]

The formation of δ, γ' and γ'' phases was hardly observed on as built samples. From a theoretical point of view the formation of such phases cannot occur during the cooling of the SLM layers because the cooling rate is very high and most of the niobium is blocked in the inter-dendritic compounds, thus impeding especially to form γ''. However, according to Tian et al.[45], the thermal cycles that the material undergoes during the following laser scans can cause a partial dissolution of the eutectic products and the diffusion of Nb towards the core of the dendrites. Then the following thermal cycles can act as repeated aging treatments that lead to a diffuse precipitation of small particles of γ''.[45]

Based on the outcome of the above-mentioned study, we can reasonably expect that the very fine particles dispersed within the cell cores (highlighted by red dotted circles in figure 2-c) are γ'' phases formed due to sequential heatings that take place during the repeated deposition of the following layers. Conversely, the typical plate-like δ phase is at all absent in the as built material.

3.1.2. Solutioned Microstructure

Since the purpose of this study is to maximize the oxidation resistance of SLM Inconel 718, it is extremely important to guarantee that all elements that can play a role in preventing dramatic oxidation of this alloy can be effectively solved and uniformly distributed within the γ matrix. From this point of view both Ti and Nb effectively participate in the formation of high temperature thermally grown protective oxide and it is therefore essential to dissolve these formed precipitates, independently by their nature, and to destroy the marked segregation patterns generated during SLM. Therefore, a dedicated post heat treatment has to be developed. The post heat treatment of SLM Inconel 718 provides several microstructural modifications. Independently by time and temperature combinations applied, the contours between laser tracks on the x-y plane and melt pools on the z plane are still partially visible (figures 3-5). However, they progressively become more blurred with the increase of temperature and of treatment duration. Nevertheless, crystalline grains preserve the memory of the as built preferential directionality along the building direction independently by the solutioning conditions applied.

3.1.2.1. Microstructure solutioned at 980°C

Samples solutioned at 980 °C have grain boundaries completely decorated by inter-granular constituents and still visible intra-granular patterns of the as built microstructure (**figure 3**). In the regions between adjacent laser tracks and melt pools the local internal stress level is very high[28] and at these locations recovery and partial recrystallization are favored thus forming fine grains. On the other hand, on the edges between laser tracks and melt pools rippled grain boundaries (see white dotted circles in the optical images of figure 3) can be observed due to the recovering process. Such feature was reported also by Zhang et al. after a solutioning at 980 °C for 1 hour and double aging.[20]

Independently by the applied soaking time, samples solutioned at 980 °C exhibited the presence of newly formed precipitates with a plate-like morphology (see SE FESEM images in figure 3) located mainly at grain boundaries, but also within grains.

The SE FESEM micrographs reported in figure 3 also show the occurrence of partial dissolution of the eutectic products (carbides and Laves) at the inter-dendritic boundaries. However, small equiaxed constituents are still present along the boundaries of cells inside each grain, giving clues to the fact that at this solutioning temperature only partial dissolution of the eutectic phases occurs. As discussed above, a new coarser constituent with plate-like morphology can be clearly detected at grain boundaries, with a larger size, and inside the grain, with a smaller size. Such plate-like precipitates were also observed by Zhang et al.[20], after solutioning at 980°C and double aging, and were identified as δ phase through TEM analysis. The theoretical solvus temperature of the δ phase is a function of local Nb content ranging between ca. 1,005°C (corresponding to the 5.06% Nb) and 1,015°C (corresponding to the 5.41% Nb contain).[46] Therefore at 980 °C, i.e. below its solvus temperature, due to favorable conditions the δ phase can nucleate and grow first at grain boundary and then also inside the grain.

These observations are also in good agreement with Wang et al.[13] that performed a solution treatment at 980 °C for 1 hours followed by double aging on Inconel 718 alloy produced via SLM. Actually, the δ-Ni_3Nb phase doesn't form during the additive manufacturing process due to the limited availability of Nb in the matrix, but such phase can form as soon as Laves phases and other Nb-rich compounds are dissolved upon post heat treatment. Similar mechanisms are proposed also by Popovich et al.[47] and Qi et al.[22]

The soaking time at 980°C does not modify the nature of microstructural features achieved, but, as discussed below, affects the level of dissolution achieved.

3.1.2.2. Microstructure solutioned at 1065°C

Samples solutioned at 1,065 °C exhibited a more effective dissolution of eutectic products. However, dissolved phases are here not substituted by the δ phase like in samples solutioned at 980 °C. This is a consequence of the fact that the temperature of the treatment applied here is above the solvus range of δ-phase. Due to the dissolution process, the columnar intra-granular patterns of the as built material are no more detectable (**figure 4**). Nevertheless, many undissolved equiaxed microstructural constituents are still present both at grain boundaries and inside grains. As in the case of samples treated at 980 °C, it is possible to observe a partial recrystallization that leads to the formation of smaller grains in the regions between laser tracks and melt pools.

Through SE FESEM images it is possible to observe that grain boundaries are decorated with a large number of relatively coarse constituents, even though their amount is lower with respect to what was observed on samples solutioned at 980 °C (compare the FESEM micrographs reported on figures 3 and 4 as reference). However, these coarse intergranular constituents weren't detected so far, neither in the as built samples nor in the low temperature solutioned ones. Therefore, one can conclude that these particular constituents form and grow during this relatively high temperature solutioning step. Another assumption that can be derived is that, although different in nature the inter-granular constituents are still effective in impeding grain coarsening through a pinning mechanism.[21] Small precipitates of the intra-granular type are also present in these samples. According to their morphology, they are supposed to be the residues of the inter-dendritic eutectic products, i.e. carbides and Laves phases.

Tucho et al. reported a similar microstructure on Inconel 718 samples produced by SLM and heat treated at 1100°C for 1 hour.[48] Using TEM and EDS analysis these authors were able to identify the presence of carbides, small (20-150 nm) precipitates rich in Nb, Ti, Al, O and C, small (< 100 nm) Laves phases and aluminum oxide particles. In that work, the bigger intergranular precipitates were identified as carbides. As far as the nanometric intra-dendritic

γ'' phase (shown in figure 2-c) observed in our present work are concerned, in 1065°C solutioning state they are completely dissolved.

3.1.2.3. Microstructure solutioned at 1200°C

The solution treatment at 1200 °C leads to a complete recrystallization and to a marked increase in the grain size as it can be seen in **figure 5**. The particular texture formed during the SLM process is almost completely eliminated, however the memory of grains directionality still persists. As discussed below, it is also possible to see that a complete dissolution of all second phases formed during the building process can't be achieved even with such a high solutioning treatment.

The SE FESEM micrographs in figure 5 reveal that grain boundaries (indicated by black arrows) are almost completely free of second phases. However, in the intra-granular regions there are still some clusters of coarser carbides (see for example the one indicated by white arrows in the FESEM image in the right panel of figure 5) which form along the previous location of the grain boundaries, probably as a consequence of local enrichment in Nb, Mo and Ti in these zones. As re-crystallized grain boundaries are no more constrained by the presence of inter-granular phases, they tend to markedly coarsen.

3.2. Second phases assessment

As discussed qualitatively in previous sections, within the microstructure of heat treated SLM Inconel 718 it's possible to detect and treat by image analysis quantitative data referring to the various populations and to relate them to the solutioning process applied. Some of these precipitates are residuals of the eutectic products (carbides and Laves phases) located at inter-dendritic boundaries. Other precipitates are formed during the solutioning treatment as inter- and intra-granular δ phase at 980°C and as intergranular carbides at higher solutioning temperatures. The results of the image analysis are given in terms of average volume fraction for each range of their dimensional characteristic, measured as linear size L of the precipitates

according to eq. 1. An example of image analysis treatment along with the relative size distribution and cumulative line of precipitates detected is shown in **figure 6**. This analysis directly gives a rough estimation of the overall volume fraction of all the second phases dispersed in the matrix, independently by their nature. From this analysis one can derive that the solutioning step always reduces the global volume fraction of precipitates. This result was somehow expected, but it is worthwhile to note that even with the highest temperature applied (1200°C) the solutioning process is not complete. This gives clear clues of the high thermal stability of as built precipitates. The graph clearly shows that the overall volume fraction of precipitates always decreases with solutioning temperature, but it is slightly affected by its duration, especially when the temperature is above the δ-phase solvus and dissolution process dominates on re-precipitation ones. See the discussion below on each population role for further details.

Apart from the overall precipitates fraction assessment, by considering the different size classes and their relative locations, one can draw conclusions on the effect of solutioning parameters on the specific microstructural constituents. Due to the inherent limited sensitivity of the method the value of volume fraction derived from the image analysis doesn't take into account the ultra-fine nanometric intradendritic precipitates present in the as built sample (see as reference figure 2-c). Therefore, the data treatment on as built sample is not reported hereby. Conversely, the size distributions of the precipitates detected in solutioned samples are reported in figures from 7 to 9. The first point reported in the plots always refers to the precipitates with a linear size ≤20 nm, i.e. those evaluated using only the five images at 75 kX magnification. As for all the other dimensional ranges, average volume fractions and the cumulative volume fractions were calculated using all the ten SE FESEM images collected for each treatment condition.

As far as samples solutioned at 980 °C are concerned, the size distributions plots are given twice in order to distinguish the role of precipitates respectively with and without plate-like

morphology, i.e. precipitated δ-phase. To treat separately these two populations, each object detected in the images was considered to have plate-like morphology, when it had a dimension ≥20 pixels and it had a ratio between its two main axes ≥4. Apart from this criterion, it is worthwhile to note that some care has to be applied in evaluating the size of the plate-like objects, because the same precipitate can appear bigger or smaller depending on its orientation with respect to the examined surface.

By analyzing the derived size distributions, it is possible to note that in samples solutioned at 980 °C the relative volume fraction of precipitates smaller than 80 nm almost doubles when passing from 1 hour to 2 hours of heat treatment. This can be positive as it results in the formation of finer precipitates, which are typically considered favorable in terms both of mechanical properties and of solving alloying elements into the matrix, which is in turns beneficial for oxidation resistance. The formation of this population of fine precipitates can be explained by the fact that during heat treatment the metastable Laves phases at the inter-dendritic boundaries are progressively dissolved with consequent increase in the local content of Nb dissolved into the matrix at the contours between dendritic cells. This can provide the nucleation and growth of new fine stable phases that can be reasonably considered as carbides according to their size and morphology. Further to such fine population of precipitates, it is also very clear that solutioning at 980°C provide the formation of second type precipitates population with size included within 400 and 550 nm. **Figures 7-b** and **7-c** give clues to the fact that these relatively coarse precipitates are mainly plate-like δ-phases and that as the soaking time at 980°C increases the contribution of this type of precipitates become predominant at this size range. Summarizing these observations, one can conclude that solutioning at 980°C for two hours is from one hand beneficial as it results in the formation of fine and dispersed carbides, but on the other hand detrimental as it results in the formation of relatively coarse δ-phases, that entrap Nb and limit its availability for oxidation protection purposes.

At 1065 °C solutioning temperature, independently by the soaking time the precipitates size distribution has a single peak on fine sizes, i.e. ≤80 nm. The fraction of relatively coarser precipitates is almost suppressed at this solutioning temperature. This is consistent with the fact that, as earlier discussed, δ-phase is completely dissolved and that no further coarser carbides precipitate at this temperature. Although, the size distribution is only slightly modified by increasing the soaking time from 1 hour to 2 hours, the overall fraction of precipitates is still slightly reduced by increasing the time (see cumulative curves in **figure 8-a**). This can be ascribed to the proceeding of metastable phases dissolution. Nevertheless, it is worthwhile to note that a slight increase of the volume fraction of precipitates larger than 450 nm was detected passing from 1 hour to 2 hours of heat treatment at 1065 °C. According to their relatively coarse size and globular morphology, these precipitates are probably carbides that form at high temperature. At this solutioning temperature, this process of high temperature carbides formation is very limited, but at higher temperatures this process can be more effective and lead to detrimental effect.

Upon solutioning at 1200 °C (**figure 8-b**) the overall volume fraction of precipitates detected in the treated samples is strongly reduced with respect to the other two investigated solutioning temperatures. This is due to a more efficient dissolution of inter-dendritic precipitates and destroying of segregations patterns.

During the heat treatment at high temperature, the volume fraction of precipitates larger than 370 nm is reduced by prolonging the treatment from 1 hour to 2 hours, but the volume fraction of precipitates lower than 130 nm markedly increases. This is probably due to a re-precipitation mechanism caused by the important release in solid solution of those elements previously blocked in metastable segregations that were formed during SLM solidification. As a consequence of this process, although slightly the overall volume of precipitates detected when solutioning at 1200°C increases with the soaking time.

Figure 9 compares at fixed soaking time the effect of solutioning temperature on precipitates size distribution. We can thus conclude that increasing the temperature always provides more effective dissolution of as built precipitates. Newly precipitated phases can be formed, but at 1065 and 1200°C their contribution is very limited. At 1065°C, although dissolution process is not complete, the major precipitates present are very fine (lower than 100 nm) and can be reasonably considered to be carbides. At 1200°C apart from the increased grain size, some coarse precipitates are formed. For these reasons, 1200°C solutioning is not promising. Increasing the soaking time is especially effective at 1065°C as it further reduces the overall volume fraction of precipitates at each size. Therefore, according to the precipitates dissolution processes the most promising treatment is 1065°C for 2 hours.

3.3. Vickers Microhardness Measurements

Microhardness measurements on solutioned samples were performed to have a further indirect clue of the effectiveness of as built precipitates dissolution process. A total of 10 microvickers indentations were performed for each sample. The average microhardness obtained on the not solutioned samples is of 368 ± 8 $HV_{0.01}$. As it is expected, the solution treatment leads to a reduction of the hardness of the sample due to the general coarsening of the microstructures (this mechanism is especially effective at 1200°C) and the partial dissolution of precipitates (this mechanism is more efficient as the solutioning temperature increases). In **figure 10-a** the average values of Vickers microhardness and the respective 95% confidence intervals of the measurements collected on the solutioned samples are compared with the as built one.

From figure 10-a it can be seen that the decrease of the Vickers microhardness is more pronounced as the solutioning temperature increases. In particular, a marked reduction was detected after the heat treatment at 1200 °C as a consequence of the concurrent grain coarsening and precipitates dissolution. Solutioning time less affects the microhardness levels. However, the microhardness behavior is particularly in agreement with the proposed interpretations of

microstructural evolution with temperature and time. The recorded slight microhardness increase at 980 °C with soaking time can be ascribed to the formation of δ phases. On the other hand, the microhardness reduction with soaking time recorded at 1065 °C can confirm that a progressive dissolution of the prior precipitates occurs by prolonging the soaking time. When solutioning at 1200 °C the microhardness after 1 hour and 2 hours of heat treatment is almost unaltered as grain coarsening is predominant on precipitates effect at this temperature.

To further confirm that hardness is mainly controlled by the volume fraction of precipitates and by the grain size, **figure 10-b** shows the strong correlation existing between the Vickers microhardness and the detected volume fraction for samples solutioned at 980 and 1065 °C. In figure 10-b it is also very clear that microhardness of the samples treated at 1200 °C is only slightly limited affected by the precipitates volume fraction, that become negligible. As discussed earlier at such a high solutioning temperature the predominant effect on microhardness level is the marked grain growth.

3.4. Oxidation Test

In **figure 11** the collected data during the oxidation test are reported in terms of squares of mass gain $(\Delta m/A)^2$ as a function of exposure time at the oxidation environment (850°C in calm air). It's worthwhile to note that, after the isothermal exposure, all the samples have gained in mass due to the oxide scale growth. A loss of mass or other signs of spallation or evaporation of the formed scale were never detected giving clues to the fact that the adherence of the thermally grown oxide layer onto the substrate is sufficiently high to guarantee an effective protection from further oxidation.

Greene and Finfrock report three different oxidation regimes in Inconel 718.[5] For exposures below 900°C (first regime) a period of transient run-in oxidation of about 24 hours occurs and, then, the further growth of the oxide is very steady and slow. For exposures between 900 and 1300°C (second regime) a parabolic law provides a good description of the mass gain behavior

with time. For higher temperatures exposure (third regime) the failure of the protective scale occurs, thus not protective oxide scale is formed. As long as the oxide scale is not porous and does not tend to evaporate or detach from the substrate, the parabolic law can be used to describe the oxide growth:

$$\left(\frac{\Delta w}{A}\right)^2 = k_p \cdot t \qquad (2)$$

where Δw is the mass gain at the end of the time t of the oxidation run, A is the total surface area and k_p is a costant related to the material and that describes the kinetic of a passivating oxide growth. The parabolic law was derived from the first Fick's law by Tammann, Pilling and Bedworth under the follow simplifying hypothesis:[49] the growth of the oxide occurs by atomic diffusion of species with constant diffusivity through the as formed layer; the effects of the electric field through the forming oxide on the diffusion of the species can be ignored; the concentration of the species along the oxide scale is stationary and its value at the metal/oxide and the oxide/atmosphere interfaces doesn't depend on the scale thickness.

The phenomena involved in the oxidation of Inconel 718 is definitely more complex with respect to the simple model of Tammann, Pilling and Bedworth mostly because of the presence of many alloying elements beside Cr that can have a role in the oxidation behavior, e.g. as Fe, Ti, Al and Nb. Furthermore, the strong microstructural and composition heterogeneity of SLM produced Inconel 718 discussed in the previous sections can affect the formation of the scale especially during the initial stage of the oxidation. The parabolic law assumes a constant value of k_p, however an initial transient stage of oxidation occurs[50] [51] in which a continuous protective film of oxide is not formed yet and so the rate of oxidation is high. The actual value of k_p decreases during the transient period until it stabilizes at a steady state value when all the exposed surface is completely covered by a uniform oxide scale. Then the further stationary oxidation becomes a totally diffusion controlled process. As far as the SLM Inconel 718 is considered, it can be assumed that the duration of the transient oxidation stage is also tightly

related to the compositional in-homogeneities. The content of chromium available for the formation of the protective layer of chromia is lower in the inter-dendritic regions due to microsegregation occurred during the SLM solidification. Furthermore, the presence of a large number of eutectic products in these zones can slow down the formation of a continuous protective scale.

For these reasons, the heat treatment set up was focused on removing segregation patterns and effectively dissolving especially deleterious as built Nb-rich precipitates. Therefore, the most promising solutioning preliminary at 1065°C for 2 hours was applied on all samples to be subjected to the isothermal oxidation runs.

The data collected until 351 hours of exposure (circle points in figure 11) were fitted with a linear regression line using the least square method and imposing the intercept to zero. Although 850°C would fall into the first regime of oxidation, the parabolic law fits very accurately the recorded data. The obtained value of the constant k_p is $(2.7 \pm 0.6)\cdot10^{-4}$ $mg^2cm^{-4}h^{-1}$. A low k_p value is a reliable quality indicator of the oxidation behavior, because it relates to a slow growth of the oxide scale and, as a consequence, to a slow consumption of Cr from the alloy matrix. This means that a potentially longer life at service conditions can be guaranteed for the SLM Inconel 718. The k_p value calculated in the current study for 1065°C, 2 hours, solutioned SLM Inconel 718 is much lower than that recorded in a similar oxidation test run at 850°C until 100 hours by Jia and Gu ($1.6\cdot10^{-2}$ $mg^2cm^{-4}h^{-1}$) on as built SLM Inconel 718 alloy.[15] This gives clues to the fact that optimized solutioning can markedly improve the oxidation resistance of SLM Inconel 718.

In the current study it was also possible to extrapolate the oxidation behavior of solutioned SLM Inconel 718 for very long thermal exposures, according to the procedure described in the Experimental Procedures section. By applying this procedure two further oxidation data for 755 and 908 hours exposure at 850°C in calm air were added to the analysis. The values of mass gain gathered after these further oxidation runs are also reported in figure 11 (triangle points).

These data lay on the previously obtained regression line demonstrating that the same parabolic law holds also for such a long oxidation run.

The general morphology of the oxide on the solutioned SLM Inconel 718 after 908 hours is shown in the FESEM micrographs reported in **figure 12** using Backscattered Electron mode. The superficial scale is very thin (ca. 3 μm) and well adherent to the metallic matrix. A certain level of internal oxidation is detectable in the sub-surface zone (ca. 10 μm deep from the surface). The internal oxidation pattern preferentially develops along the grain boundaries.

Apart from surface scale, microstructural modifications of the alloy after a long exposure at 850°C can be observed too. These modifications are consequences of the already discussed service aging that can be expected for the specific application as SLM high temperature heat exchanger. In particular, a large number of δ-phase precipitates with plate-like morphology develops in the entire alloy matrix forming Widmanstätten patterns with different orientations between grains. Other coarser δ-phases form along the boundaries of the columnar grains (see spectrum 6 on **figure 13**).

The effect of the δ-phase on the alloy performances is controversial: the incoherency with the matrix and the plate morphology of these precipitates increase the brittleness and furthermore δ compounds reduce the availability of Nb for the formation of the γ' and γ'' strengthening phases leading to a detrimental effect on the mechanical properties. However, the δ phase is also reported to give some advantageous effects related to the prevention of the grain growth and its pinning function at the grain boundaries[46] that avoid grain slide with consequent improvement of the creep resistance. Furthermore, a crack deflection mechanism was also proposed[52] related to the presence of plate-like δ with consequent enhancement of the high temperature stress rupture properties. The abundant δ phase formation must be taken into account carefully when long service periods at the temperature of 850°C are expected to be

accompanied by heavy external mechanical loads. In our study, only oxidation resistance was required for the SLM Inconel 718 and, therefore, such service precipitated δ phase is not critical. As far as the oxide scale is concerned, it is possible to observe the following features:

- in the intra-granular regions the superficial scale is thinner and at the metal/oxide interface a quasi-continuous layer of about 1 μm (it appears in bright contrast in figure 12-b) is formed;
- in the inter-granular regions the superficial oxide protrudes outwardly and the quasi-continuous layer is interrupted by the formation of inter-granular internal oxides that develop at a depth of ca. 10 μm;
- the oxide scale can be divided in two layers: an inner dense layer that is uniform (in back scattered scanning mode the uniform grey level corresponds to a uniform chemical composition) and an outer with few isolated porosities and non-uniform chemical composition.

The EDS analysis performed on the oxide layers are reported in figure 13. An estimation of the atomic percentages of the detected elements is also given, however these values are only indicative because the interaction volume below the electron beam is larger than the examined features and therefore the signals of the surrounding matrix is altering the exact elementary assessment. Nevertheless, the reported analysis provides a semi-quantitative information about the composition of the scale.

According to this analysis, we can conclude that the outer layer is mainly composed by chromium oxide with a minor presence of Al, Ti and Fe (spectrum 1 on figure 13). A larger amount of Fe and Ni was detected on the metal particles embedded in this layer, therefore these particles are supposed to be portions of the original metallic alloy that remained entrapped due to the inward growth of the oxide scale at metal/oxide interface. Along grain boundaries the

internal oxide scale is richer in Ti close to the metal/oxide interface, whereas is enriched in Al as moving farer from such interface.

Giggins and Pettit classified the oxidation behavior of superalloys on the base of the Ni-Cr-Al ternary system:[51] in this scheme Inconel 718 belongs to the group II of alloys that in oxidizing environment form an external layer of chromia (Cr_2O_3)[53] and a subscale or discontinuous particles of alumina (Al_2O_3) beneath. The chromia layer can act as an effective protective layer until 1000°C, but at higher temperatures evaporation occurs through the $Cr_2O_{3\,(s)} + 3/2\,O_2 \rightleftarrows 2CrO_{3\,(g)}$ reaction.[54] [55] At 850°C the outer chromia layer is stable and therefore the growth of the oxide scale is mainly controlled by the inward diffusion of O^{2-} anions and by the outward diffusion of Cr^{3+} cations through the oxide scale. The oxides sequence observed in this study is in good agreement with what reported by Giggins and Pettit[51] and Chen et al.[56] and it can be explained by considering the different oxygen affinities of the alloying elements: Al has the highest oxygen affinity, i.e. the highest tendency to oxidize, followed by Ti and Cr. An oxygen concentration gradient develops along the subsuperficial layer because the O^{2-} anions inward diffusion becomes more complicated as they move farer from the environment/oxide interface. Therefore the chromia scale develops until the oxygen content falls below the threshold value for the oxidation of Cr at 850°C. At inward locations, where oxygen level is not high enough to oxidize Cr, Ti can start to oxidize. Finally, at even more inward locations where oxygen content is even lower and Ti is not further oxidized, only Al is able to form oxides along the grain boundaries.

EDS analysis (spectrum 3 on figure 13) also reveals that the quasi-continuous thin layer formed at the metal/oxide interphase is mainly composed by Ni and Nb. A quite similar intermetallic Ni_3Nb layer is actually reported by Delaunay et al.[57] and by Al-Hatab et al.[58], who suggested that the Nb-rich interlayer can have an important influence on the oxidation behavior because it can act as a diffusion barrier for both anionic and cationic diffusion, thus slowing the thickening of oxidation products. Al-Hatab et al. reported a value of the k_p constant of the

parabolic law recorded during cyclic oxidation of Inconel 718 alloy at 850°C until 170 hours equal to $7.7 \cdot 10^{-4}$ $mg^2cm^{-4}h^{-1}$[58], i.e. the same order of magnitude obtained in test reported here (although our value is almost 3 times lower).

Based on our observation the Nb-rich interlayer seems to be able to slow down the penetration of the O^{2-} anions in the intragranular zones, thus reducing the formation of internal oxides. However, in the inter-granular zones the interlayer is interrupted (how it is shown in figure 12-b) and thus internal titanium and aluminum oxides can form along grain boundaries, that are preferential diffusion paths.[59] The outward growth of the superficial chromia is also faster in correspondence of the grain boundaries because of the local higher diffusivity of the Cr^{3+} cations, this cause the formation of superficial protrusions visible in figure 12-a.

4. Conclusions

In this study the solution treatment of SLM Inconel 718 was studied in order to maximize the hot oxidation resistance of the alloy. To this purpose the solution process was studied to improve the microstructures derived from the SLM process and, in particular, to homogenize segregated regions, to recover the microstructural heterogeneities at the contours between laser tracks and melt pools and to dissolve the large amount of Laves phases and carbides derived from the eutectic transformations occurred during SLM solidification.

To assess the capability of solutioning process to positively affect microstructural features, different trials of solutioning was performed using time and temperature combinations.

Microstructural analysis and Vickers microhardness measurements were performed according to the different solutioning conditions.

According to our results solutioning at 1200°C is not advisable because it leads to severe grain coarsening and following large loss of the mechanical properties without giving marked benefits in terms of solutioning efficiency. At 980 °C the formation of δ phase cannot be avoided because the solvus temperature of this phase is higher. The temperature value of

1065 °C has been identified as the best in term of solutioning efficiency and the soaking time of 2 hours was selected in order to promote the maximal dissolution of as built precipitates, without causing excessive grain growth.

The long oxidation run (up to 908 hours) carried out on solutioned SLM Inconel 718 has shown a regular parabolic increase of the mass due to oxidation when exposed at 850 °C in air. The parabolic trend of the mass gain per unit of area is the consequence of an effective diffusion controlled process that takes place thanks to the formation of a dense, protective and stable oxide scale on the surface of the alloy. The k_p value of the parabolic law detected in this study is lower than the results available in the literature for oxidation runs at the same temperature, demonstrating the good oxidation resistance of SLM produced Inconel 718 at the service temperature of interest and the beneficial effect of the identified solution treatment.

Received: ((will be filled in by the editorial staff))
Revised: ((will be filled in by the editorial staff))
Published online: ((will be filled in by the editorial staff))

[1] A. Simchi, *Mater. Sci. Eng., A* **2006**, *428*, 148.

[2] D. Manfredi, F. Calignano, E. P. Ambrosio, M. Krishnan, R. Canali, S. Biamino, M. Pavese, E. Atzeni, L. Iuliano, P. Fino, C. Badini, *Metall. Ital.* **2013**, *105*, 15.

[3] D. S. Thomas, S. W. Gilbert, in *National Institute of Science and Technology* **2014**, http://dx.doi.org/10.6028/NIST.SP.1176.

[4] INCONEL Alloy 718, in *Special Metals Corporation (*www.specialmetals.com*)* **2007**, *Publication Number SMC-045*.

[5] G. A. Greene, C. C. Finfrock, *Oxid. Met.* **2001**, *55*, 505.

[6] J. F. Radavich, in *Superalloy 718 - Metallurgy and Applications* (Ed.: E. A. Loria), The Minerals, Metals & Materials Society **1989**, *229*.

[7] M. G. Burke, M. K. Miller, in *Superalloys 718, 625 and Various Derivatives* (Ed.: E. A. Loria), The Minerals, Metals & Materials Society **1991**, *337*.

[8] C.-M. Kuo, Y.-T. Yang, H.-Y. Bor, C.-N. Wei, C.-C. Tai, *Mater. Sci. Eng., A* **2009**, *510–511*, 289.

[9] EOS NickelAlloy IN718, in *EOS GmbH - Electro Optical Systems* (www.eos.info), Material data sheet **2014**.

[10] D. H. Smith, J. Bicknell, L. Jorgensen, B. M. Patterson, N. L. Cordes, I. Tsukrov, M. Knezevic, *Mater. Charact.* **2016**, *113*, 1.

[11] X. Gong, K. Chou, in *Annual Meeting Supplemental Proceedings*, The Minerals, Metals & Materials Society **2015**, *461*.

[12] I. A. Roberts, C. J. Wang, R. Esterlein, M. Stanford, D. J. Mynors, *Int. J. Mach. Tools Manuf.* **2009**, *49*, 916.

[13] Z. Wang, K. Guan, M. Gao, X. Li, X. Chen, X. Zeng, *J. Alloys Compd.* **2012**, *513*, 518.

[14] Q. Jia, D. Gu, *J. Alloys Compd.* **2014**, *585*, 713.

[15] Q. Jia, D. Gu, *Opt. Laser Technol.* **2014**, *62*, 161.

[16] A. Keshavarzkermani, M. Sadowski, L. Ladani, *J. Alloys Compd.* **2018**, *736*, 297.

[17] M. Sadowski, L. Ladani, W. Brindley, J. Romano, *Addit. Manuf.* **2016**, *11*, 60.

[18] S. Gribbin, J. Bicknell, L. Jorgensen, I. Tsukrov, M. Knezevic, *Int. J. Fatigue* **2016**, *93*, 156.

[19] G. Marchese, M. Lorusso, S. Parizia, E. Bassini, J. -W. Lee, F. Calignano, D. Manfredi, M. Terner, H. -U Hong, D. Ugues, M. Lombardi, S. Biamino, *Mater. Sci. Eng., A* **2018**, *729*, 64.

[20] D. Zhang, W. Niu, X. Cao, Z. Liu, *Mater. Sci. Eng., A* **2015**, *644*, 32.

[21] E. Chlebus, K. Gruber, B. Kuznicka, J. Kurzac, T. Kurzynowski, *Mater. Sci. Eng., A* **2015**, *639*, 647.

[22] H. Qi, M. Azer, A. Ritter, *Metall. Mater. Trans. A* **2009**, *40*, 2410.

[23] F. Calignano, F. Monaco, M. Calandri, G. Marchese, E. P. Ambrosio, M. Lorusso, D. Manfredi, D. Ugues, in *Proceeding of 6th International Conference on Additive Technologies* **2016**, 383.

[24] G. Marchese, E. Bassini, M. Calandri, E. P. Ambrosio, F. Calignano, M. Lorusso, D. Manfredi, M. Pavese, S. Biamino, P. Fino, *Met. Powder Rep.* **2016**, *71*, 273.

[25] G. Marchese, G. Basile, E. Bassini, A. Aversa, M. Lombardi, D. Ugues, P. Fino, S. Biamino, *Mater.* **2018,** *11*, 1, https://doi.org/10.3390/ma11010106.

[26] W. Shifeng, L. Shuai, W. Qingsong, C. Yan, Z. Sheng, S. Yusheng, *J. Mater. Process. Technol.* **2014**, *214*, 2660.

[27] F. Liu, X. Lin, C. Huang, M. Song, G. Yang, J. Chen, W. Huang, *J. Alloys Compd.* **2011**, *509*, 4505.

[28] F. Liu, X. Lin, G. Yang, M. Song, J. Chen, W. Huang, *Opt. Laser Technol.* **2011**, *43*, 208.

[29] Y. L. Kuo, S. Horikawa, K. Kakehi, *Mater. Des.* **2017**, *116*, 411.

[30] V. A. Popovich, E. V. Borisov, A. A. Popovich, V. Sh. Sufiiarov, D. V. Masaylo, L. Alzina, *Mater. Des.* **2017**, *114*, 441.

[31] J. Cao, F. Liu, X. Lin, C. Huang, J. Chen, W. Huang, *Opt. Laser Technol.* **2013**, *45*, 228.

[32] G. P. Dinda, A. K. Dasgupta, J. Mazumder, *Scr. Mater.* **2012**, *67*, 503.

[33] L. L. Parimi, G. Ravi, D. Clark, M. M. Attallah, *Mater. Charact.* **2014**, *89*, 102.

[34] Y. Chen, F. Lu, K. Zhang, P. Nie, S. R. E. Hosseini, K. Feng, Z. Li, P.K. Chu, *Mater. Des.* **2016**, *105*, 133.

[35] L. Ladani, J. Razmi, S. F. Choudhury, *J. Eng. Mater. Technol.* **2014**, *136*, 1.

[36] D.M. Stefanescu, R. Ruxanda, in *Fundamentals of Solidification*, ASM Handbook - Metallography and Microstructures, Vol. 9 (Ed: ASM International), **2004**, 71.

[37] K. N. Amato, S. M. Gaytan, L. E. Murr, E. Martinez, P. W. Shindo, J. Hernandez, S. Collins, F. Medina, *Acta Mater.* **2012**, *60*, 2229.

[38] J. Kundin, L. Mushongera, H. Emmerich, *Acta Mater.* **2015**, *95*, 343.

[39] G. A. Knorovsky, M. J. Cieslak, T. J. Headley, A. D. Romig Jr, W. F. Hammetter, *Metall. Trans. A* **1989**, *20A*, 2149.

[40] S. G. K. Manikandan, D. Sivakumar, K. Prasad Rao, M. Kamaraj, *Mater. Charact.* **2015**, *100*, 192.

[41] Ch. Radhakrishna, K. Prasad Rao, *J. Mater. Sci.* **1997**, *2*, 1977.

[42] D. A. Porter, K. E. Easterling, in *Phase Transformations in Metals and Alloys*, 2nd edition (Ed: Chapman & Hall), London, UK **1992**.

[43] X. Wang, K. Chou, *Addit. Manuf.* **2017**, *18*, 1.

[44] F. Brenne, A. Taube, M. Pröbstle, S. Neumeier, D. Schwarze, M. Schaper, T. Niendorf, *Progr. Addit. Manuf.* **2016**, *1*, 141.

[45] Y. Tian, D. McAllister, H. Colijn, M. Mills, D. Farson, M. Nordin, S. Babu, *Metall. Mater. Trans. A* **2014**, *45*, 4470.

[46] S. Azadian, L. Y. Wei, R. Warren, *Mater. Charact.* **2004**, *53*, 7.

[47] V. A. Popovich, E. V. Borisov, A. A. Popovich, V. Sh. Sufiiarov, D. V. Masaylo, L. Alzina, *Mater. Des.* **2017**, *131*, 12.

[48] W. M. Tucho, P. Cuvillier, A. Sjolyst-Kverneland, V. Hansen, *Mater. Sci. Eng., A* **2017**, *689*, 220.

[49] H. A. Miley, *J. Electrochem. Soc.* **1942**, *81*, 391.

[50] D. K. Das, V. Singh, S. V. Joshi, *Mater. Sci. Technol.* **2003**, *19*, 695.

[51] C. S. Giggins, F. S. Pettit, *J. Electrochem. Soc.* **1971**, *118*, 1782.

[52] G. Sjoberg, N. G. Ingesten, R. G. Carlson, in *Superalloys 718, 625 and Various Derivatives* (Ed.: E. A. Loria), The Minerals, Metals & Materials Society **1991**, *603*.

[53] D. M. England, A. V. Virkar, *J. Electrochem. Soc.* **1999**, *146*, 3196.

[54] D. Caplan, M. Cohen, *J. Electrochem. Soc.* **1961**, *108*, 438.

[55] C. S. Tedmon. Jr., *J. Electrochem. Soc.* **1966**, *113*, 766.

[56] J. H. Chen, P. M. Rogers, J. A. Little, *Oxid. Met.* **1997**, *47*, 381.

[57] F. Delaunay, C. Berthier, M. Lenglet, J.-M. Lameille, *Microchim. Acta* **2000**, *132*, 337.

[58] Kh. A. Al-Hatab, M. A. Al-Bukhaiti, U. Krupp, M. Kantehm, *Oxid. Met.* **2011**, *75*, 209.

[59] V. B. Trindade, U. Krupp, Ph. E. -G. Wagenhuber, H. -J. Christ, *Mater. Corros.* **2005**, *56*, 785.

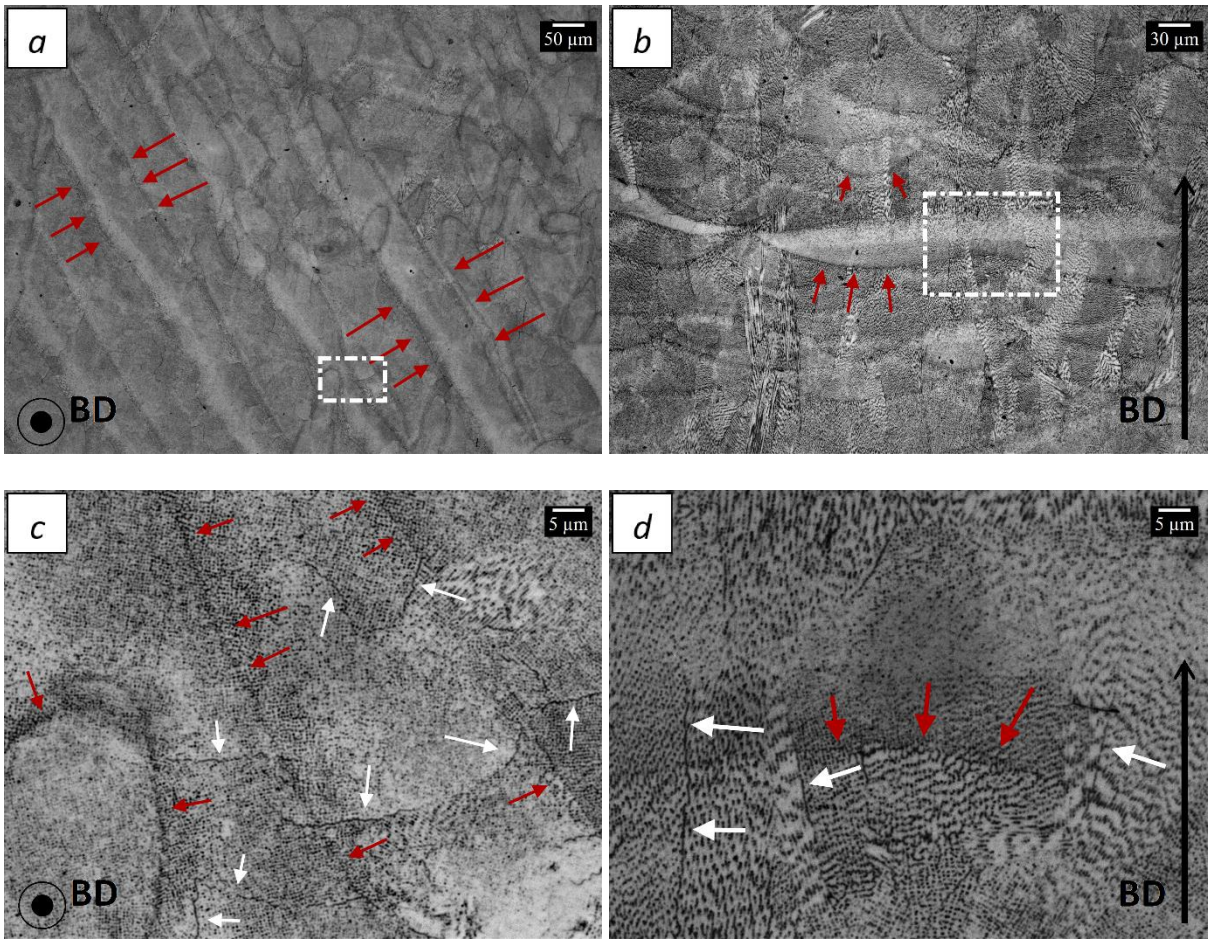

Figure 1. Optical micrographs of etched as built Inconel 718 at increasing magnifications with identification of Building Direction (BD). Boundaries between the laser tracks on x-y plane (a and c) and arc-shaped melt pools contours on the z plane (b and d) are indicated by red arrows. Grain boundaries are indicated by white arrows in c and d. The white dotted boxes in a and b indicate the magnification zones shown respectively in c and d.

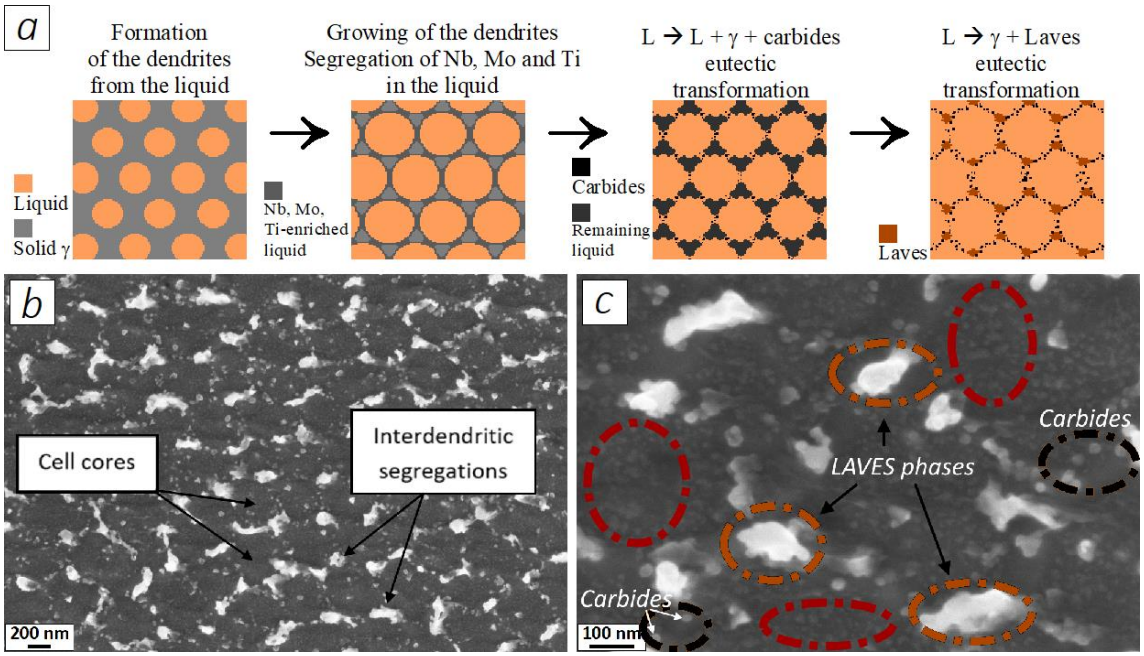

Figure 2. Schematic model of the solidification path and resulting distribution of the eutectic products: carbides and Laves phases (a). Secondary Electrons FESEM micrographs on the x-y plane of the as built Inconel 718 showing a cellular structure (b) with interdendritic precipitates (within brown and black dotted circles in figure c) and the presence of a high density of ultra-fine precipitates in the cell cores (within red dotted circles in figure c).

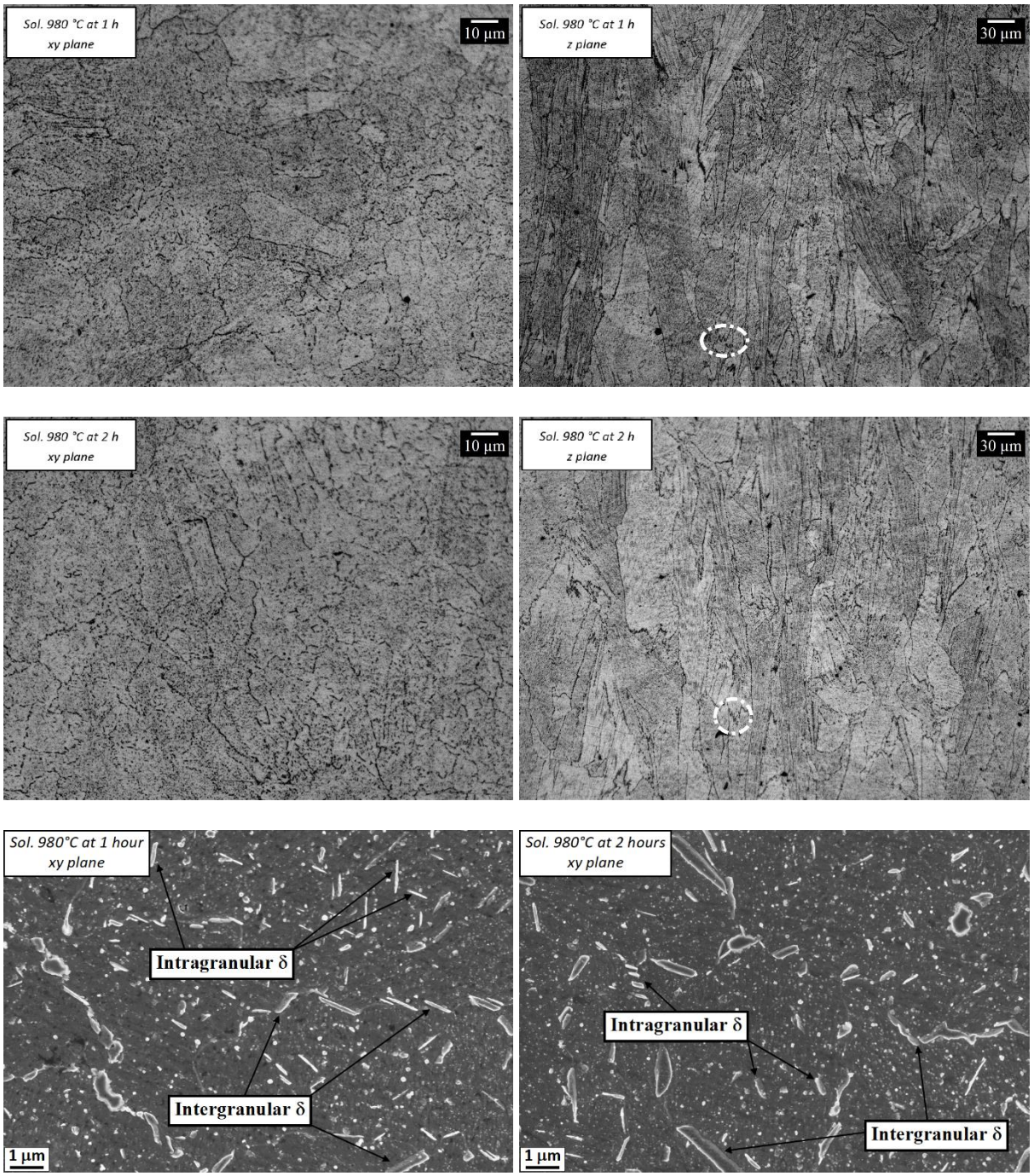

Figure 3. Optical (first 4 panels) and Secondary Electrons FESEM (last 2 panels) micrographs on the xy plane and on the z plane of the solutioned SLM Inconel 718 at 980°C for 1 hour and 2 hours. The dotted white circles indicate examples of rippled grain boundaries.

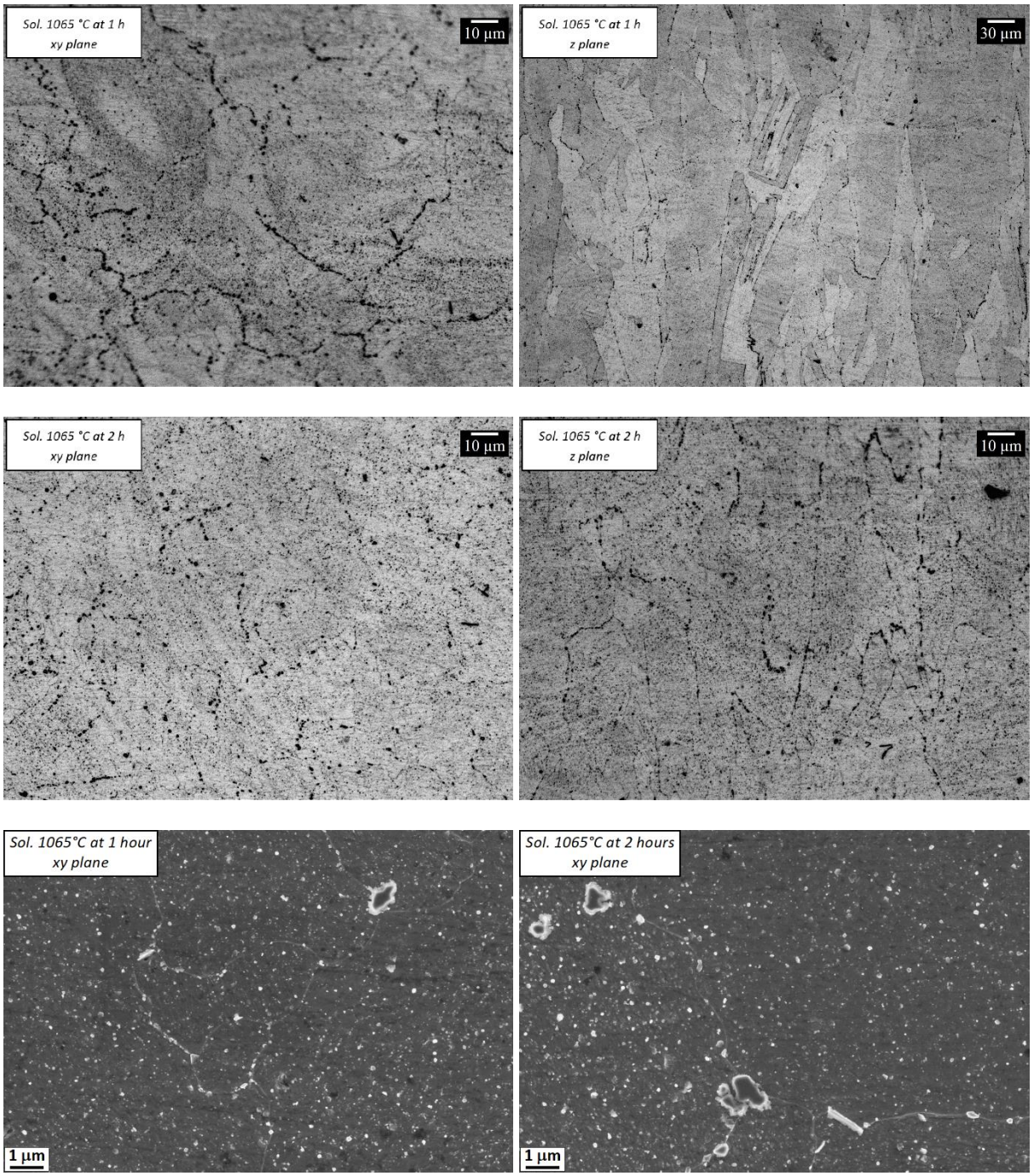

Figure 4. Optical (first 4 panels) and Secondary Electrons FESEM (last 2 panels) micrographs on the xy plane and on the z plane of the solutioned SLM Inconel 718 at 1065°C for 1 hour and 2 hours.

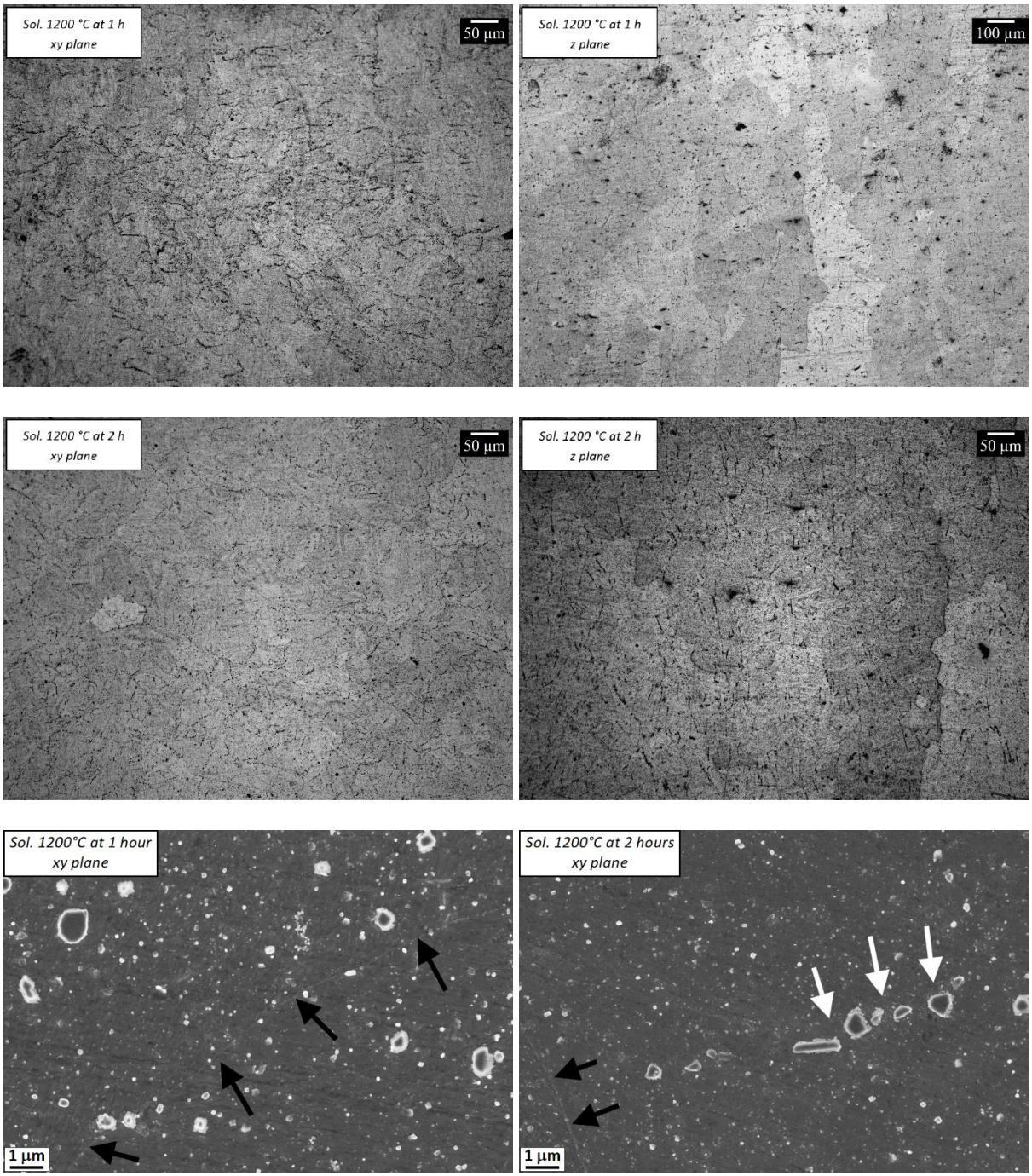

Figure 5. Optical (first 4 panels) and Secondary Electrons FESEM (last 2 panels) micrographs on the xy plane and on the z plane of the solutioned SLM Inconel 718 at 1200°C for 1 hour and 2 hours. In the FESEM images, black arrows indicate residual grain boundaries and white arrows indicate a cluster of carbides, probably originated at previous grain boundary.

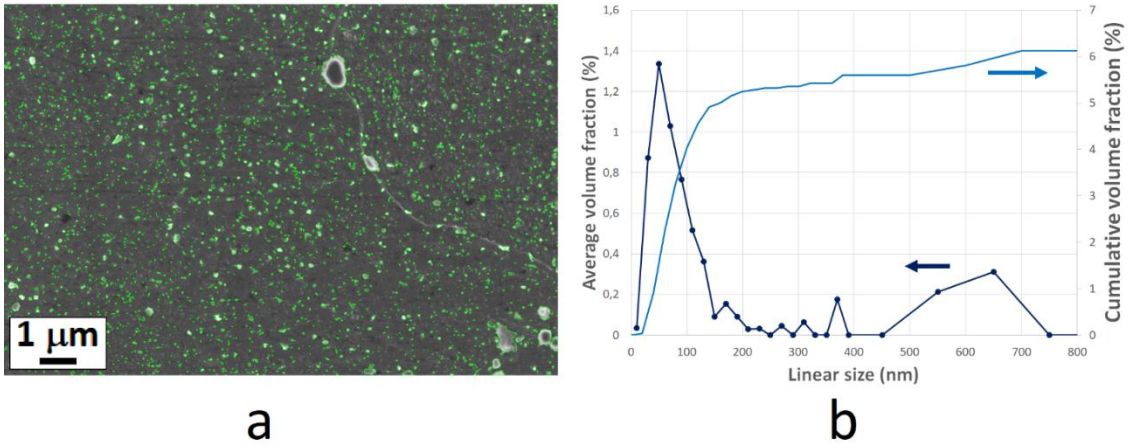

Figure 6. Example of Secondary Electrons FESEM image analysis as treated by image analysis process (a) and the related precipitates size distribution (b). This reference image was taken on a sample solutioned at 1065°C for 2 hours.

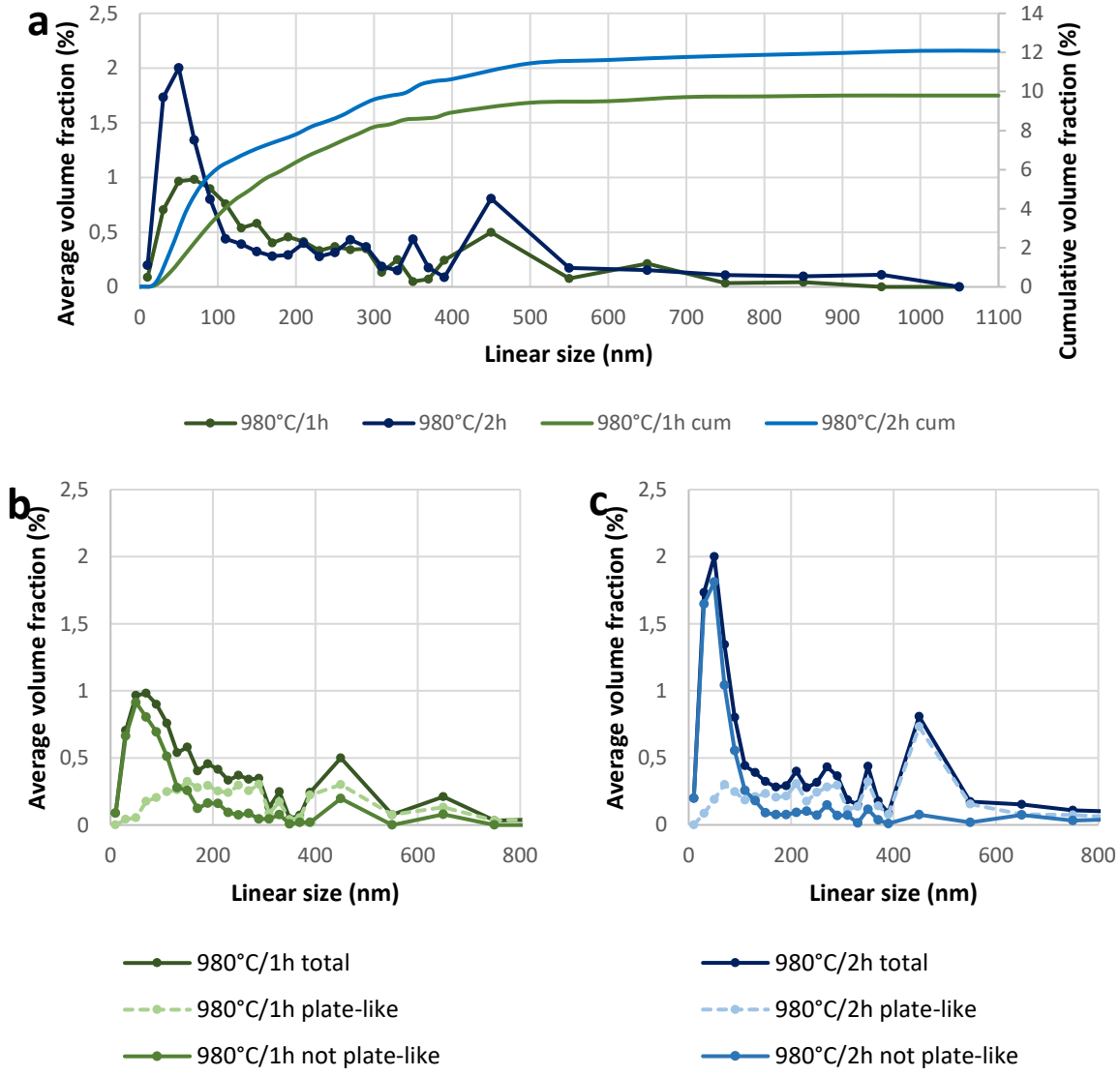

Figure 7. Overall precipitates size distribution derived on samples solutioned at 980°C for 1 hour (green lines) and 2 hours (blue lines) with related cumulative curves (a); size distributions of precipitates with plate-like morphology and without plate-like morphology after 1 hour (b) and 2 hours (c) of solutioning at 980°C.

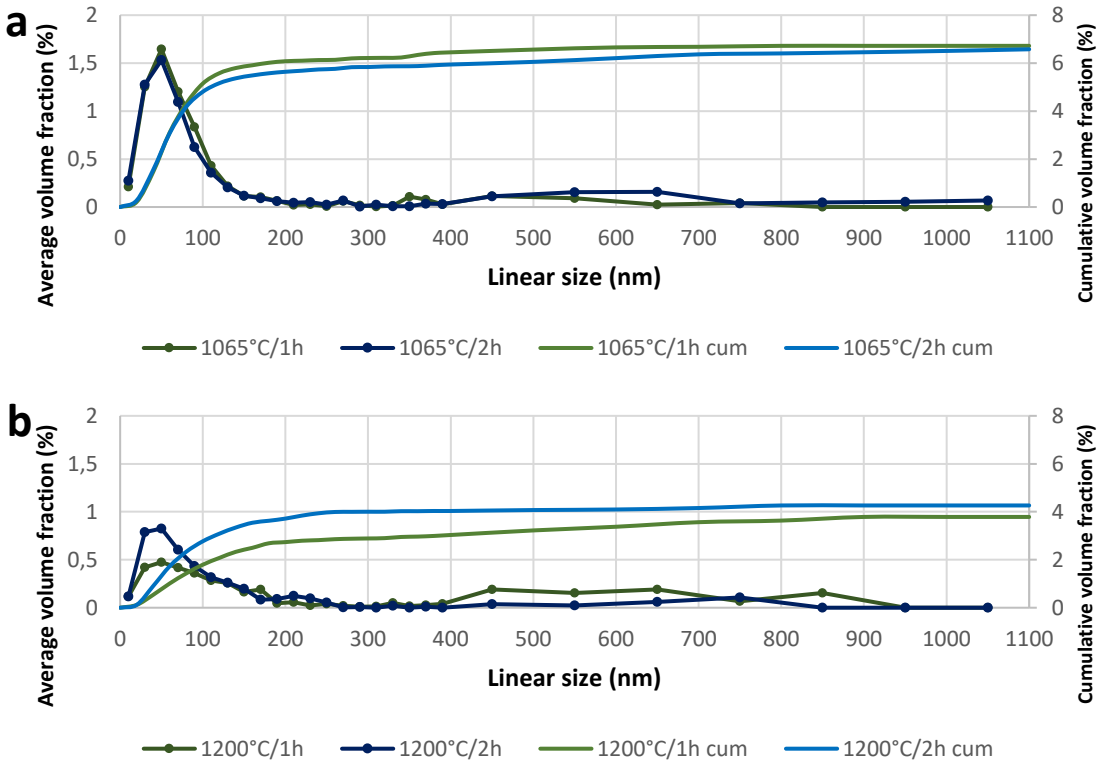

Figure 8. Precipitate size distributions derived on samples solutioned at 1065°C (a) and at 1200°C (b) for 1 hour (green lines) and 2 hours (blue lines) with related cumulative curves.

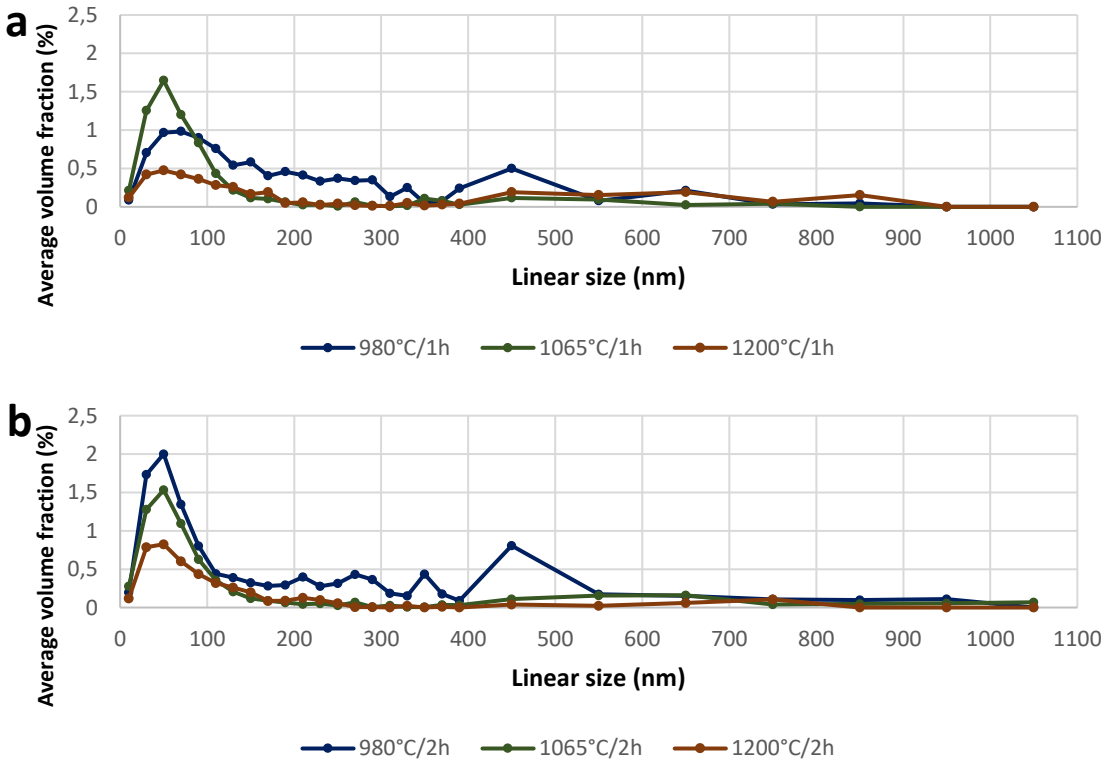

Figure 9. Comparison of precipitate size distributions derived on samples solutioned for 1 hour (a) and 2 hours (b) at different solutioning temperature: 980 °C (blue lines), 1065 °C (green lines) and 1200 °C (orange lines).

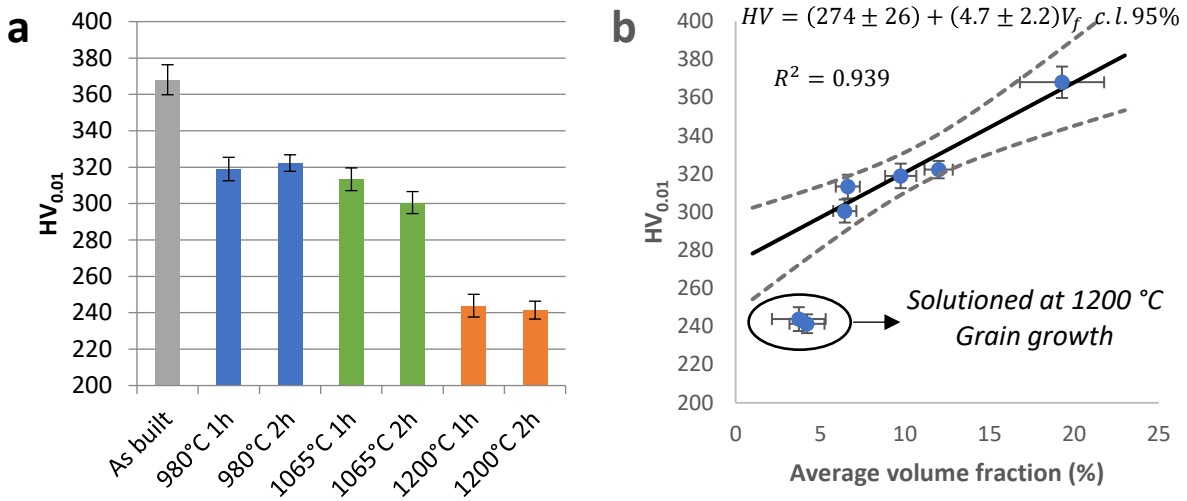

Figure 10. Vickers microhardness (a) of the as built and the solutioned samples (the vertical error bars refer to 95% confidence intervals) and correlation (b) between Vickers microhardness and the volume fraction of precipitates (the horizontal error bars refer to standard deviations of the volume fractions calculated on recorded data). The regression line with relative 95% confidence band is derived excluding the data relative to the samples solutioned at 1200 °C for which a loss of hardness is observed due to marked grain growth.

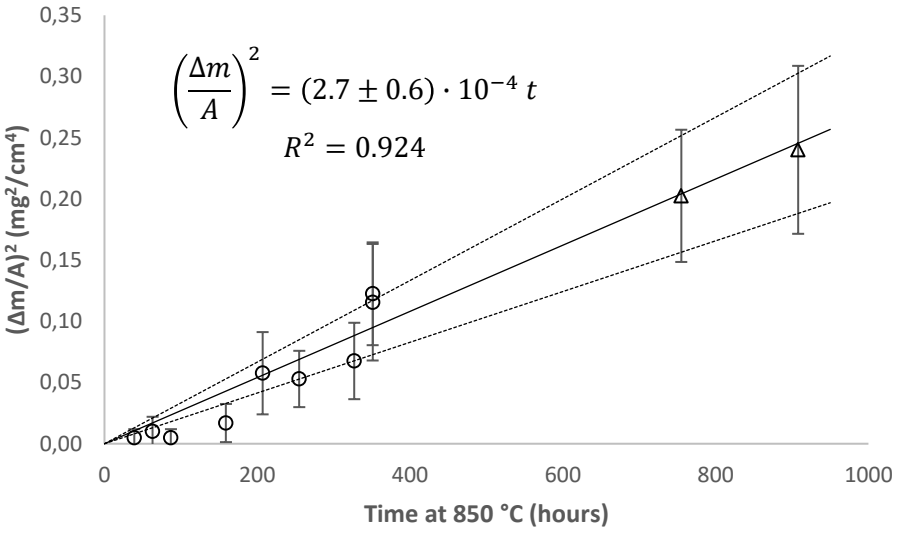

Figure 11. Squares of mass gain per unit of exposed area versus oxidation time plot of solutioned SLM Inconel 718 and relative zero-intercept linear regression with 95% confidence range. The error bars indicate the propagated measurement uncertainties.

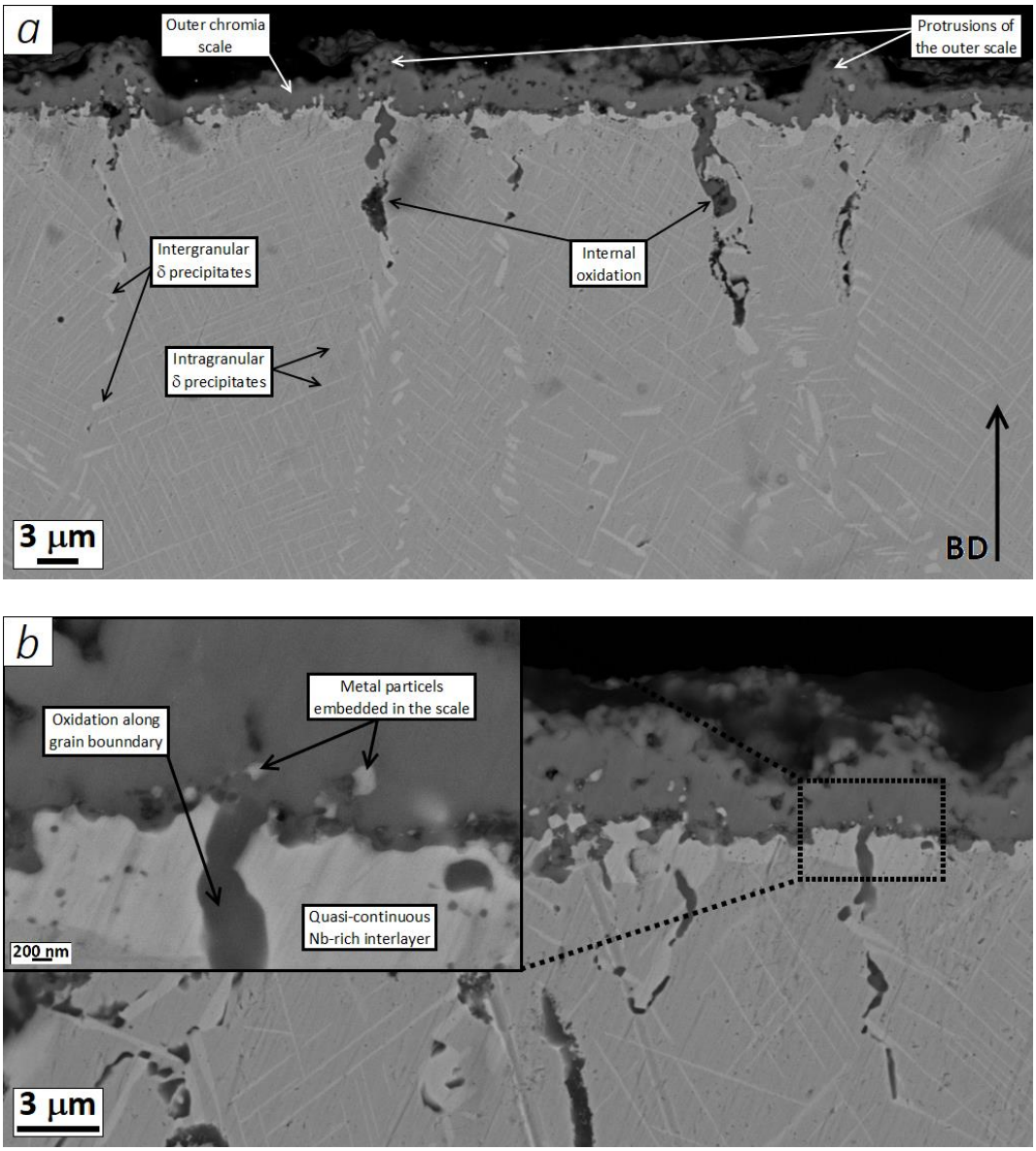

Figure 12. FESEM micrographs in back scattered electrons (BSE) mode of the oxide scale on solutioned SLM Inconel 718 after 908 hours at 850 °C; the black arrow in panel a indicates the building direction during the SLM process. Nature of phases is derived by EDS analysis discussed below.

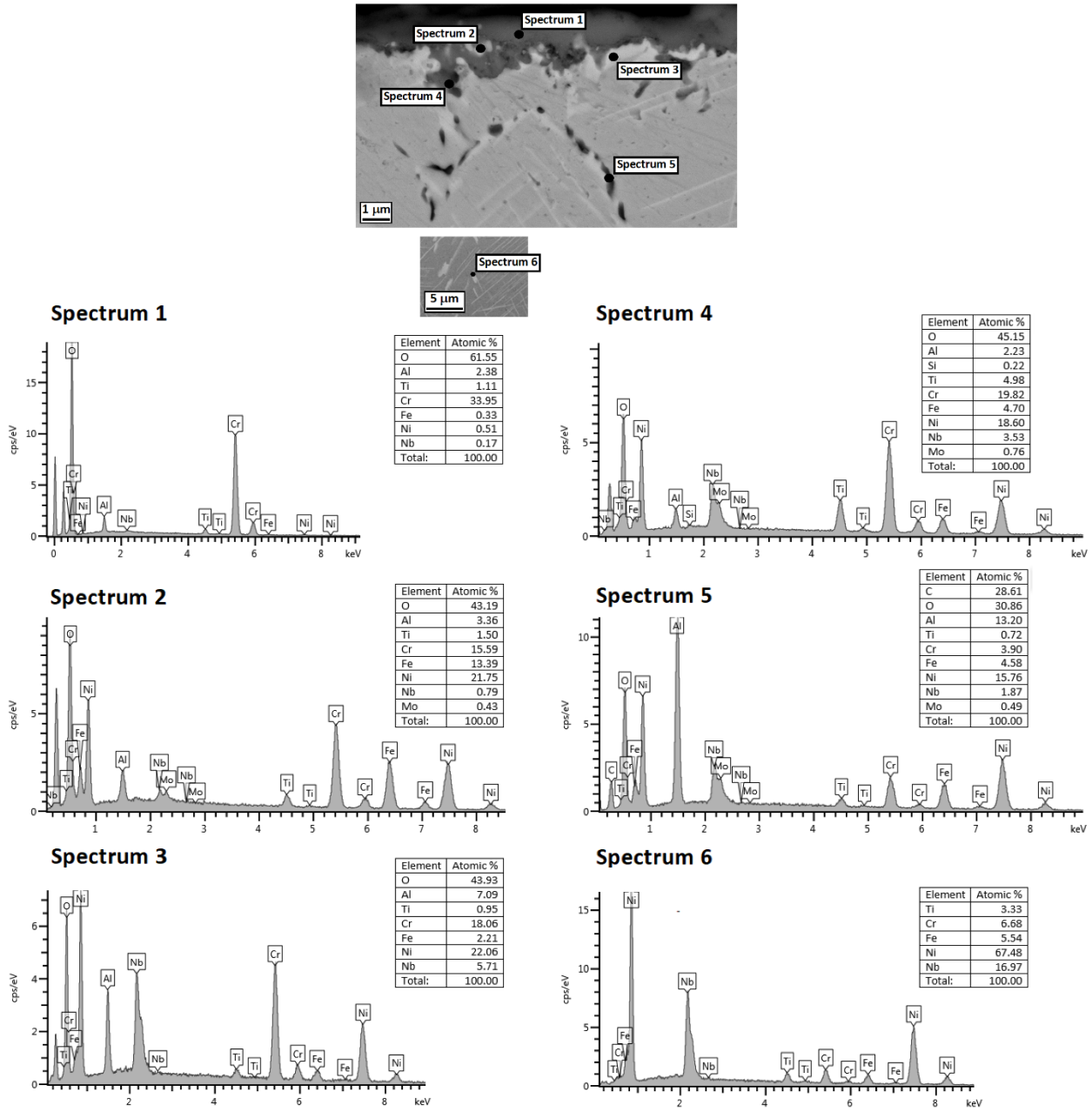

Figure 13. Spot EDS analysis on: superficial oxide layer (spectrum 1); particles embedded in it (spectrum2); thin interlayer at metal/oxide interface (spectrum 3); internal oxides rich in Ti (spectrum 4); deeper internal oxides rich in Al (spectrum 5); intergranular precipitate (spectrum 6).

Table 1. Nominal chemical composition in wt. % of Inconel 718 EOS powders used [9].

Ni	**Cr**	**Nb**	**Mo**	**Ti**	**Al**	**Fe**
50 - 55	17 – 21	4.75 – 5.5	2.8 – 3.3	0.65 – 1.15	0.2 – 0.8	
Co	**Cu**	**C**	**Si + Mn**	**P + S**	**B**	*balance*
< 1	< 0.3	< 0.08	< 0.35	< 0.015	< 0.006	

Table 2. List of the six sets of solutioning parameters investigated within the study.

Temperature [°C]	Time [minutes]
980	*60*
	120
1065	*60*
	120
1200	*60*
	120

Table of contents

In this paper, we show the microstructure of Inconel 718 Ni based superalloy produced by Selective Laser Melting (SLM) in the as built condition and its evolution after different solutioning treatment. The final goal of the study is to optimize the solutioning treatment in view of the hot oxidation resistance of the alloy at the temperature of the final application (850°C). Therefore, the result of a long (908 hours) oxidation test at 850°C of the solutioned material is also reported.